



Cite as
Nano-Micro Lett.
(2020) 12:6

Received: 30 September 2019
Accepted: 20 November 2019
Published online: 16 December 2019
© The Author(s) 2019

Photocatalytic H₂ Evolution on TiO₂ Assembled with Ti₃C₂ MXene and Metallic 1T-WS₂ as Co-catalysts

Yujie Li¹, Lei Ding¹, Shujun Yin¹, Zhangqian Liang¹, Yanjun Xue¹, Xinzhen Wang¹ ✉, Hongzhi Cui¹ ✉, Jian Tian¹ ✉

Yujie Li and Lei Ding have contributed equally to this work.

✉ Xinzhen Wang, xzwang@sdust.edu.cn; Hongzhi Cui, cuihongzhi1965@163.com; Jian Tian, jiantian@sdust.edu.cn

¹ School of Materials Science and Engineering, Shandong University of Science and Technology, Qingdao 266590, People's Republic of China

HIGHLIGHTS

- The 1T-WS₂@TiO₂@Ti₃C₂ photocatalyst is highly active for water splitting to produce hydrogen at 3409.8 μmol g⁻¹ h⁻¹.
- The Ti₃C₂ MXene and octahedral (1T) phase WS₂ act pathways transferring photogenerated electrons.

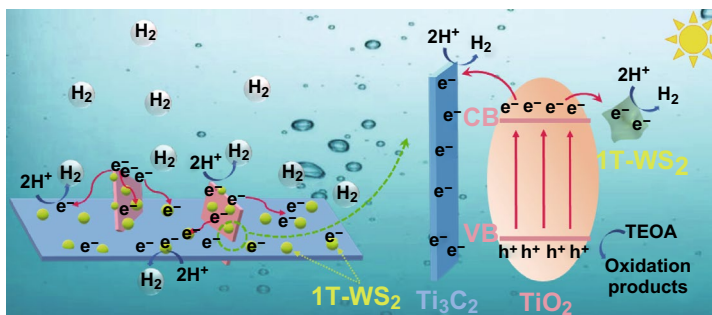
ABSTRACT The biggest challenging issue in photocatalysis is efficient separation of the photoinduced carriers and the aggregation of photoexcited electrons on photocatalyst's surface. In this paper, we report that double metallic co-catalysts Ti₃C₂ MXene and metallic octahedral (1T) phase tungsten disulfide (WS₂) act pathways transferring photoexcited electrons in assisting the photocatalytic H₂ evolution. TiO₂ nanosheets were in situ grown on highly conductive Ti₃C₂ MXenes and 1T-WS₂ nanoparticles were then uniformly distributed on TiO₂@Ti₃C₂ composite. Thus, a distinctive 1T-WS₂@TiO₂@Ti₃C₂ composite with double metallic co-catalysts was achieved, and the content of 1T phase reaches 73%. The photocatalytic H₂ evolution performance of 1T-WS₂@TiO₂@Ti₃C₂ composite with an optimized 15 wt% WS₂ ratio is nearly 50 times higher than that of TiO₂ nanosheets because of conductive Ti₃C₂ MXene and 1T-WS₂ resulting in the increase of electron transfer efficiency. Besides, the 1T-WS₂ on the surface of TiO₂@Ti₃C₂ composite enhances the Brunauer–Emmett–Teller surface area and boosts the density of active site.

KEYWORDS Photocatalytic H₂ production; Ti₃C₂ MXene; Octahedral phase WS₂; TiO₂ nanosheets; Co-catalysts

1 Introduction

Due to energy consumption and consequent environmental pollution, the generation of hydrogen (H₂) from water using solar light through semiconductors materials has aroused great attention [1–4]. Among these, TiO₂ is widely studied

owing to nontoxicity and low cost [5, 6]. However, the fast photoexcited carrier recombination restricts the TiO₂'s application, and thus numerous efforts, such as doping, co-catalyst loading and heterostructure designing, are made to improve photoexcited carrier separation [7, 8]. Among these, co-catalysts can gather carriers to improve separation and



act as active sites for H₂ production [9]. Noble metals as excellent co-catalysts have widely applied to photocatalysis. However, extreme scarcity and high price restrict their application of photocatalytic water splitting [10, 11]. Therefore, seeking an inexpensive and highly active co-catalyst is of paramount significance for achieving photocatalytic H₂ production in the future [12].

MXenes, as new 2D materials, have aroused remarkable attention because of its excellent electrical conductivity [13, 14]. For example, a 2D material with an accordion-like structure of layered Ti₃C₂ MXene can be prepared by etching Al layers from Ti₃AlC₂, in HF solution [15–17]. Due to its high electrical conductivity and unique layer morphology, Ti₃C₂ MXene is an appropriate substitute co-catalyst for noble metals for photocatalytic H₂ evolution [18].

In recent years, transition metal disulfides (TMDs), such as molybdenum disulfide (MoS₂) and tungsten disulfide (WS₂), are regarded as promising substitutes for noble metals on catalysis [19, 20]. MoS₂ and WS₂ mainly include semiconductive trigonal (2H) phase and metallic octahedral (1T) phase [21, 22]. Both experimental and theoretical research have revealed that the metallic 1T phase possesses outstanding conductivity and more active sites, which will be suitable co-catalyst for photocatalytic H₂ evolution, compared with 2H phase [23]. As one of the most popular TMDs materials, 1T phase MoS₂ has been widely studied on photocatalysis [24–26]. However, the report about 1T phase WS₂ (1T-WS₂) on photocatalytic H₂ production is still rare.

In this paper, an innovative 2D heterojunction by utilizing the metallic feature of Ti₃C₂ MXene and 1T-WS₂ is reported. A two-step hydrothermal method is used for designing the novel 1T-WS₂@TiO₂@Ti₃C₂ photocatalyst where Ti₃C₂ MXene and 1TWS₂ play important roles as electron acceptors. Firstly, TiO₂ nanosheets are in situ grown on the surface of highly conductive Ti₃C₂ MXenes to construct TiO₂@Ti₃C₂ composites by a facile hydrothermal method. Secondly, we intentionally employ the 1T-WS₂ nanoparticles evenly distribute on TiO₂@Ti₃C₂ composites' surface using a hydrothermal process. This procedure results in the construction of an efficient photocatalytic system with intimate contact among metallic Ti₃C₂ MXene, 1T-WS₂ nanoparticles, and TiO₂ NSs. The newly designed 1T-WS₂@TiO₂@Ti₃C₂ composites exhibit extremely enhanced photocatalytic H₂ evolution activity and stability owing to the novel structure.

2 Experimental Procedures

2.1 Materials

Ti₃AlC₂ powder was purchased from 11 Technology. Hydrochloric acid (HCl), sodium tetrafluoroborate (NaBF₄), hydrofluoric acid (HF, 40 wt%), tungsten chloride (WCl₆), thioacetamide (TAA), and dimethylformamide (DMF) were provided by Sinopharm.

2.2 Synthesis of Ti₃C₂ MXenes

In a typical synthesis, 1 g Ti₃AlC₂ powders were dissolved in 120 mL HF solution (40 wt%) and were stirred for 72 h. Then, the mixed solution was washed with deionized (DI) water to neutral. Lastly, Ti₃C₂ MXenes were dried at 50 °C for overnight in a vacuum oven.

2.3 Synthesis of TiO₂@Ti₃C₂ Composites

Ti₃C₂ MXenes (400 mg) and NaBF₄ (660 mg) were dissolved in 60 mL HCl (1.0 M) and were stirred for 30 min. The mixed solution was hydrothermally treated at 160 °C for 12 h. The obtained TiO₂@Ti₃C₂ composites were washed with DI water and dried at 60 °C for overnight in a vacuum oven.

2.4 Synthesis of 1T-WS₂@TiO₂@Ti₃C₂ Composites

WCl₆ (24 mg) and TAA (9 mg) were added into 50 mL DMF. Then, 100 mg TiO₂@Ti₃C₂ composites were dispersed in above solution and were stirred for 60 min. The mixed solution was hydrothermally treated at 200 °C for 24 h. The obtained 1T-WS₂@TiO₂@Ti₃C₂ composites (15 wt% WS₂) were washed with DI water and dried at 60 °C for overnight in a vacuum oven. By adjusting the adding amount of WCl₆ (16, 32, and 40 mg) and TAA (6, 12, and 15 mg), 1T-WS₂@TiO₂@Ti₃C₂ composites with other WS₂ adding amounts (10, 20, and 25 wt%) were prepared, respectively.

2.5 Characterizations

The phases of the samples were carried out using D/Max 2500PC X-ray diffraction (XRD). The surface characteristic

and structure of the samples were tested by a FEI Nano 450 high-resolution scanning electron microscope (FESEM) and a JEOL 2100F high transmission electron microscope (HRTEM). The chemical states of the products were analyzed by a Thermo ESCALAB 250XI X-ray photoelectron spectrometry (XPS). The specific surface area and pore size distribution were tested by a nitrogen adsorption–desorption apparatus (Micromeritics ASAP2020) using the Brunauer–Emmett–Teller (BET) method. The UV–Vis diffuse reflectance spectra (DRS) of the products were measured using a Hitachi UH3101 UV–Vis spectrophotometer. The photoluminescence (PL) spectra were tested by a FLS920 fluorescence.

2.6 Photoelectrochemical and Photocatalytic Activity Test

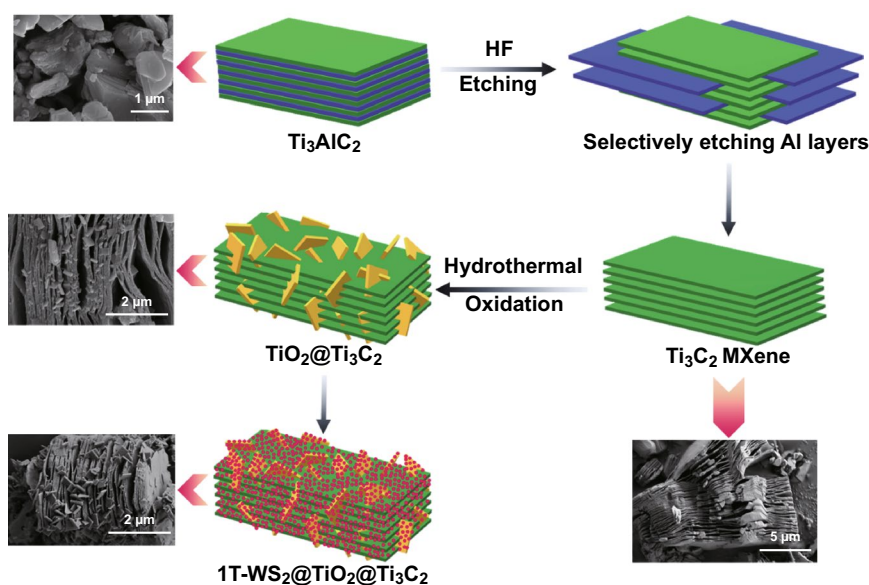
The photocatalytic activity test was measured using a Pyrex glass vessel, with a 300 W Xe arc lamp (CELHXF300) with an AM-1.5 filter as the light source. 10 mg of catalysts were added into acetone/TEOA solution (15 mL acetone + 5 mL TEOA + 80 mL DI water). The amount of generated H_2 was tested by a gas chromatograph (Techcomp GC-7920). The electrochemical impedance spectroscopy (EIS) and transient photocurrent response (PEC) of the catalysts were measured by an electrochemical workstation (CHI660D) under

a 300 W Xe arc lamp with an AM-1.5 filter in a three-electrode cell (0.5 M Na_2SO_4). Ag/AgCl electrode and Pt wire were used as reference and counter electrodes, respectively.

3 Results and Discussion

A typical synthesis route of 1T- $WS_2@TiO_2@Ti_3C_2$ composites is schematically depicted in Scheme 1. Ti_3C_2 MXenes are firstly prepared by etching Al layers of Ti_3AlC_2 MAX phase in HF solution [27]. Then, the layered Ti_3C_2 MXene provides Ti sources with the help of HCl and $NaBF_4$ for growing TiO_2 NSs across the layered Ti_3C_2 MXene. Finally, the obtained $TiO_2@Ti_3C_2$ composites are added into WCl_6 /TAA solutions at 200 °C for 24 h to introduce 1T- WS_2 co-catalysts. In this process, due to the intercalation of NH_4^+ of TAA, the space distance of WS_2 increases and 1T- WS_2 is generated [19]. The 1T- WS_2 is evenly assembled on $TiO_2@Ti_3C_2$ composites' surface to construct the ternary 1T- $WS_2@TiO_2@Ti_3C_2$ composites.

After HF etching, the most intense XRD (104) peak of Ti_3AlC_2 was disappeared, and the (002) peak of Ti_3AlC_2 at 9.52° was moved to lower 2-theta value (8.78°), which indicates the successful formation of Ti_3C_2 (Fig. S1a) [17]. The development of TiO_2 nanosheets across Ti_3C_2 MXenes by the hydrothermal oxidation of Ti_3C_2 is evidenced by the emergence of diffraction peaks of anatase TiO_2 (JCPDS No.



Scheme 1 Schematic illustration of the preparation of 1T- $WS_2@TiO_2@Ti_3C_2$ composites

21-1272) as shown in Fig. 1a. The XRD peaks appearing at 6.66° , 13.40° , and 20.10° are indexed to (002), (004), and (006) planes of 1T-WS₂ [23]. The co-existence of Ti₃C₂, TiO₂, and 1T-WS₂ indicates the successful preparation of 1T-WS₂@TiO₂@Ti₃C₂ composites. For 1T-WS₂@TiO₂@Ti₃C₂ composites with other WS₂ ratios (Fig. S1b), all the XRD peaks are well corresponding to Ti₃C₂, TiO₂, or 1T-WS₂.

The full-scale XPS spectrum of 1T-WS₂@TiO₂@Ti₃C₂ composites (Fig. 1b) displays that Ti, C, O, S, and W are dominant elements, while F element is ascribed to F⁻ ions physically adsorbed on composites from the HF solution. The Ti 2*p* spectrum is divided into four peaks (Fig. 1c). The two peaks at 464.7 (Ti–O 2*p*_{1/2}) and 459.0 eV (Ti–O 2*p*_{3/2}) are ascribed to lattice Ti–O bonds of TiO₂ [28]. The other two peaks at 461.2 (Ti–C 2*p*_{1/2}) and 455.3 eV (Ti–C 2*p*_{3/2}) are indexed to lattice Ti–C bonds of Ti₃C₂ [29]. The high-resolution Ti 2*p* XPS spectrum indicates the content of Ti₃C₂ is about 79% in TiO₂@Ti₃C₂ composites. The W 4*f* XPS spectrum of 1T-WS₂@TiO₂@Ti₃C₂ composites (Fig. 1d) can confirm the presence and relative content of 1T-WS₂. In the

W 4*f* region, the two peaks of 2H phase corresponding to W 4*f*_{7/2} and W 4*f*_{5/2} at 33.0 and 36.0 eV, respectively. Nevertheless, two extra peaks shift to lower binding energies at 32.4 and 34.6 eV, suggesting the existence of 1T-WS₂ [19, 30]. The 1T phase content is calculated about 73%, which shows that the 1T-WS₂@TiO₂@Ti₃C₂ composites are composed of lots of metallic 1T phase.

Ti₃C₂ MXenes are obtained by etching of the aluminum layer of the bulk Ti₃AlC₂ (Fig. S2a) by using HF. As shown in Fig. 2a, Ti₃C₂ MXenes present typical accordion-like multilayer structure. After hydrothermal oxidation of Ti₃C₂ MXenes, the layered Ti₃C₂ MXenes provide Ti sources for growing TiO₂ NSs inserting across the layered Ti₃C₂ MXene to form TiO₂@Ti₃C₂ composites, and further combine with WS₂ through hydrothermal reaction to get 1T-WS₂@TiO₂@Ti₃C₂ composites. Figure 2b shows that 1T-WS₂ presents nanoflake structures and agglomerate into nanoflowers. After combining with TiO₂@Ti₃C₂ composites, the 1T-WS₂ nanoparticles are evenly distributed on TiO₂@Ti₃C₂ composites' surface (Fig. 2c, d). Furthermore, 1T-WS₂@TiO₂@Ti₃C₂ composites with other WS₂ ratios (10, 20, and 25 wt%)

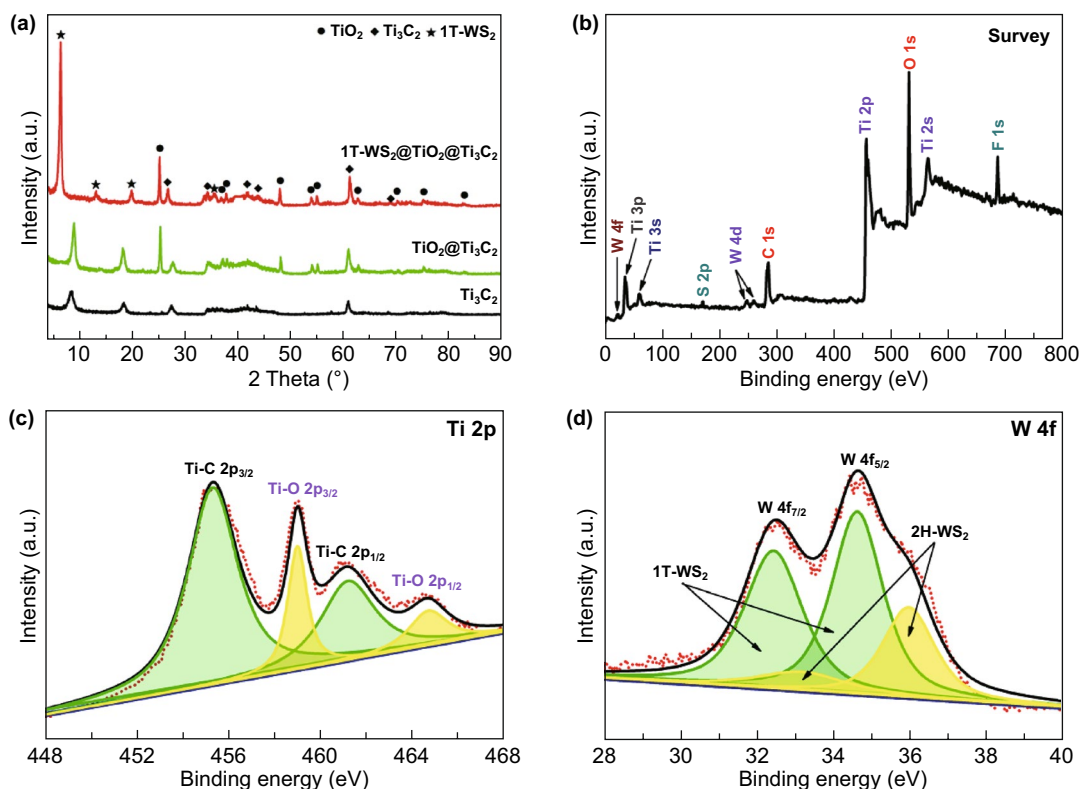


Fig. 1 a XRD patterns of Ti₃C₂, TiO₂@Ti₃C₂, and 1T-WS₂@TiO₂@Ti₃C₂ composites (15 wt% WS₂); b fully scanned XPS spectrum, c Ti 2*p*, and d W 4*f* XPS spectra in 1T-WS₂@TiO₂@Ti₃C₂ composites (15 wt% WS₂)

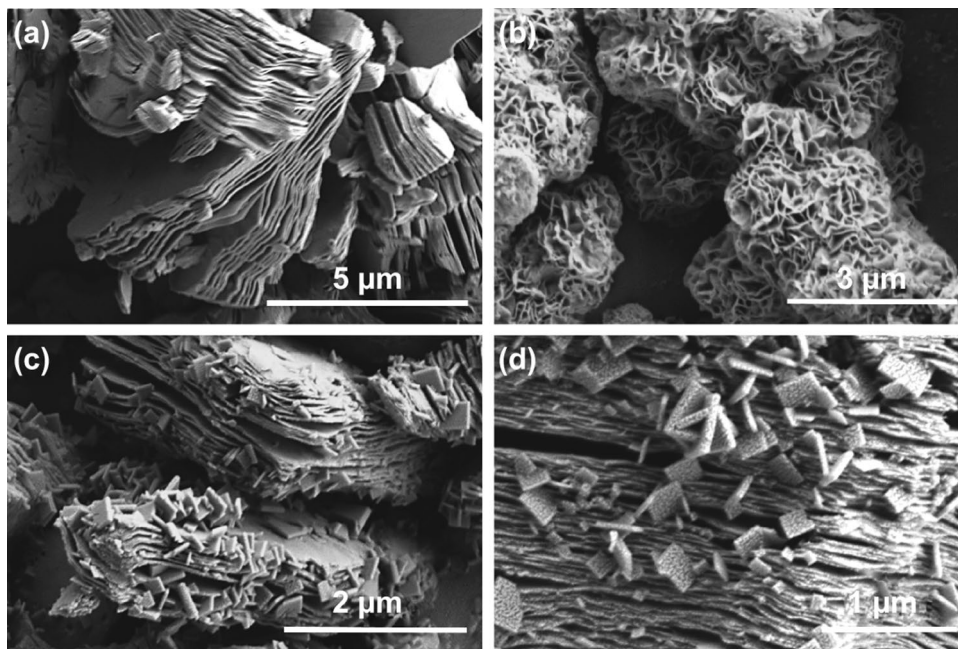


Fig. 2 SEM images of **a** Ti₃C₂ MXene, **b** 1T-WS₂, and **c, d** 1T-WS₂@TiO₂@Ti₃C₂ composites (15 wt% WS₂)

are prepared, and corresponding SEM images are displayed in Fig. S2.

The phase composition and microscopic structure of 1T-WS₂@TiO₂@Ti₃C₂ composites are characterized by TEM (Fig. 3a, b). The lattice with *d* spaces of 0.35 nm is attributed to (101) plane of anatase TiO₂ (Fig. 3b), which are same as the description of the literatures [31, 32]. The lattice spacings of 0.98 and 0.92 nm are indexed to (002) plane of

Ti₃C₂ MXene and (002) plane of 1T-WS₂ [19, 33–35] (Fig. 3b). The EDX element mappings of composites (Fig. 3c) indicate that the Ti, C, O, W, and S elements are accordantly distributed. The as-fabricated photocatalyst with superior metallic quality of Ti₃C₂ MXene and 1T-WS₂ present more effective carrier transfer and separation compared with TiO₂ NSs, and therefore, the photocatalytic performance is enhanced. The 1T-WS₂ is further confirmed by

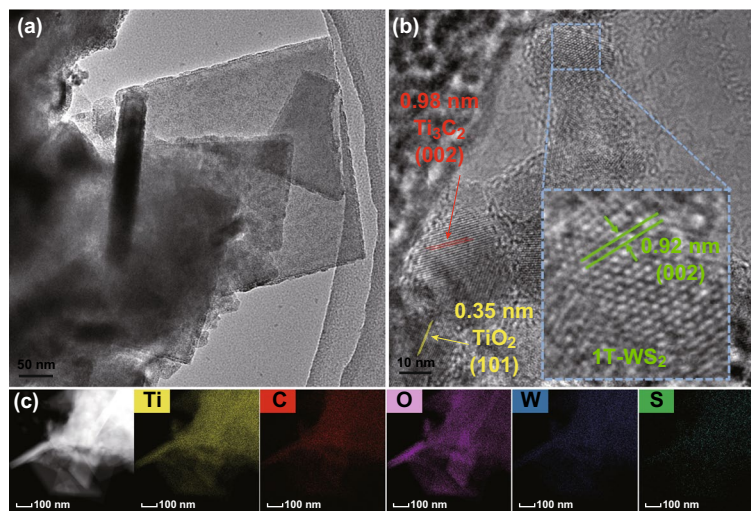


Fig. 3 **a, b** HRTEM and **c** EDX elemental mapping images of 1T-WS₂@TiO₂@Ti₃C₂ composites (15 wt% WS₂)

Raman spectroscopy (Fig. S3). Remarkably, in contrast to 2H phase WS_2 , there are no scattering peaks between 350 and 450 cm^{-1} attributed to E_{2g}^1 (in-plane) and A_{1g} (out-of-plane) in 1T- WS_2 (Fig. S3). There are also two strong peaks at low frequency range for 1T- WS_2 . One strong Raman band at 128 cm^{-1} (J_1) is attributed to W–W stretching vibrations in 1T- $\text{WS}_2@TiO_2@Ti_3C_2$ composite [21]. Besides, another additional peak at 171 cm^{-1} (J_2) is observed, which is associated with the phonon modes in the WS_2 , suggesting the existence of a considerable amount of 1T phase ingredient embedded [22]. This result further implies that the as-prepared WS_2 in 1T- $\text{WS}_2@TiO_2@Ti_3C_2$ composites is mostly 1T phase [19, 23].

To further examine the textural properties of 1T- $\text{WS}_2@TiO_2@Ti_3C_2$ composites, the isotherms and the pore size distributions are studied by N_2 adsorption–desorption measurement (Figs. 4 and S4). All of samples present type IV isotherms with H3 hysteresis loops, suggesting the presence of mesopores [36]. And the pore size distribution curves of

1T- $\text{WS}_2@TiO_2@Ti_3C_2$ composites with different WS_2 loading amounts (Fig. 4a–d inset) display that the size of major mesopores ranges from 2 to 25 nm. Compared with other samples, when the loading amount of WS_2 is 15%, the pore size distribution is relatively concentrated at 2~5 nm. The presence of such a small pore size is conducive to migration of reactant and product molecules to facilitate photocatalytic reactions. Moreover, larger nitrogen adsorption capacity indicates that more reactive sites may be provided during the reaction process, which is favorable in the enhancement of catalytic activity. The BET surface area of as-prepared 1T- $\text{WS}_2@TiO_2@Ti_3C_2$ -15%, as shown in Table S1, reveals a higher surface area ($23.334\text{ m}^2\text{ g}^{-1}$) than those of Ti_3C_2 MXene, pure 1T- WS_2 , and 1T- $\text{WS}_2@TiO_2@Ti_3C_2$ composites with other WS_2 loading amounts. In addition, as shown in Figs. 4 and S4, the BET surface area of the samples increase nonlinearly with increasing WS_2 loading. As the WS_2 loading amount increases from 10 to 15 wt%, the BET surface area of composites increases. However, further

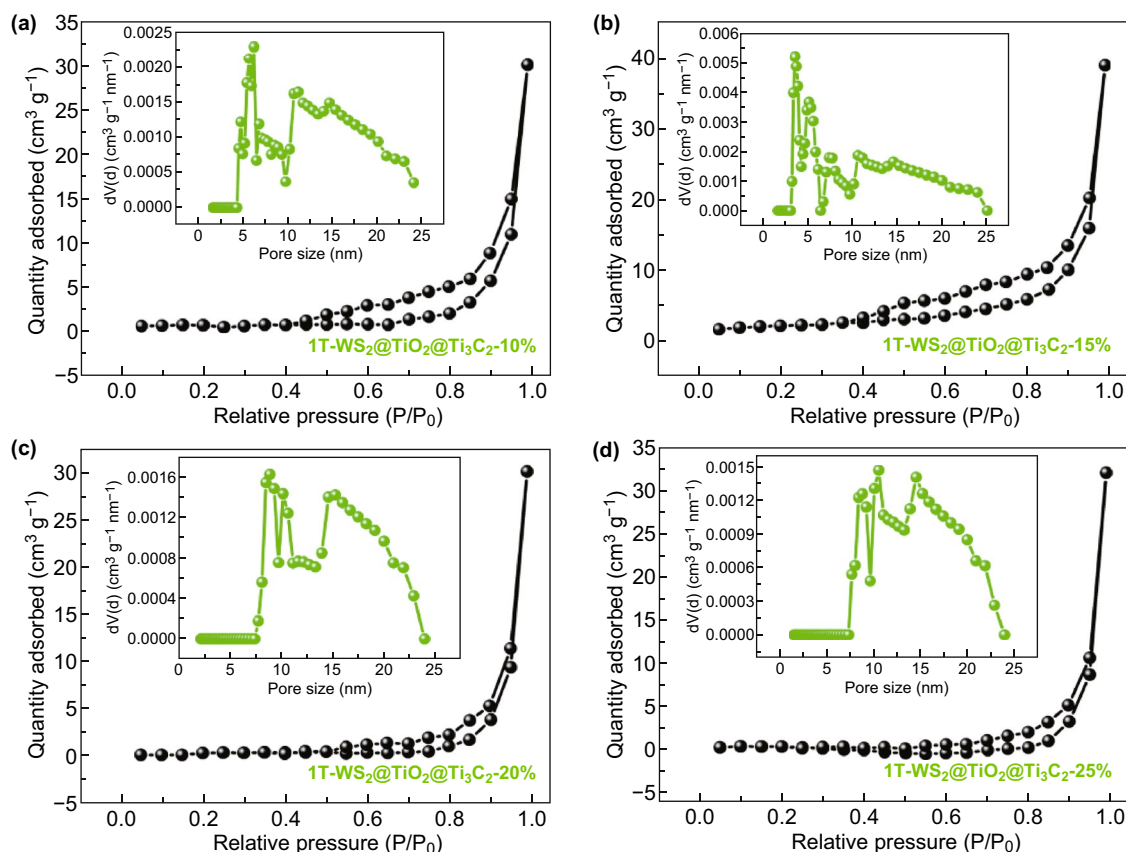


Fig. 4 N_2 adsorption–desorption isotherms and corresponding pore size distribution curves (inset) of 1T- $\text{WS}_2@TiO_2@Ti_3C_2$ composites with a 10 wt%, b 15 wt%, c 20 wt%, and d 25 wt% WS_2 ratios

increasing the loading amount of WS₂ (from 15 to 25 wt% WS₂) leads to a gradual decrease of BET surface area, which may be caused by the aggregation of WS₂ on the surface of the composites. The higher surface areas are beneficial for photocatalysis since it could provide more adsorption and active sites, thus the photocatalytic activity is improved [37].

To investigate the optical absorptivity, the UV–Vis DRS spectra of samples are measured. As shown in Fig. 5, TiO₂ NSs (curve black) have a noticeable UV light absorption, due to the nature of anatase TiO₂ [38]. Ti₃C₂ MXene (curve blue) shows UV and visible absorption as a result of the black color nature [39]. Compared with TiO₂ NSs, 1T-WS₂@TiO₂@Ti₃C₂ composites (15 wt% WS₂) display a significant absorption edge red shift and enhanced visible absorption, which is attributed to the optical absorption of

Ti₃C₂ MXene and 1T-WS₂. The increase of light absorption range of photocatalysts will be more helpful to promote the progress of photocatalytic reaction. Besides, the 1T-WS₂@TiO₂@Ti₃C₂ composites show stronger light absorption with the increase of WS₂ contents from 10 to 25 wt% (Fig. S5).

The photocatalytic performance of 1T-WS₂@TiO₂@Ti₃C₂ composites was evaluated using H₂ evolution under simulated sunlight irradiation in an aqueous acetone solution at room temperature (Fig. 6). Control experiments (Fig. S6) show that no noticeable H₂ evolution is discovered without either photocatalyst or illumination. TiO₂ NSs (Fig. 6) present limited photocatalytic H₂ activity (67.8 μmol g⁻¹ h⁻¹), arising from fast carrier recombination [40]. In view of the excellent electronic conductivity of Ti₃C₂ and 1T-WS₂, it is combined as a co-catalyst with TiO₂ NSs in order to achieve better photogenerated carrier separation and improve photocatalytic performance [41, 42]. As expected, after assembling of Ti₃C₂ and 1T-WS₂, the best photocatalytic activity is detected (3409.8 μmol g⁻¹ h⁻¹ for 1T-WS₂@TiO₂@Ti₃C₂ composites (15 wt% WS₂)), which is nearly 50 times higher than that of TiO₂ NSs. Moreover, the 1T-WS₂@TiO₂@Ti₃C₂ composites (10 wt% WS₂) present a lower photocatalytic activity than 1T-WS₂@TiO₂@Ti₃C₂ composites (15 wt% WS₂), owing to the relatively weaker solar light input. Furthermore, with the increase of WS₂ contents from 15 to 25 wt%, a reduction in the photocatalytic performance of 1T-WS₂@TiO₂@Ti₃C₂ composites is discovered. Because excess black 1T-WS₂ nanoparticles induced “shielding effect” block light to the surface of TiO₂ [43].

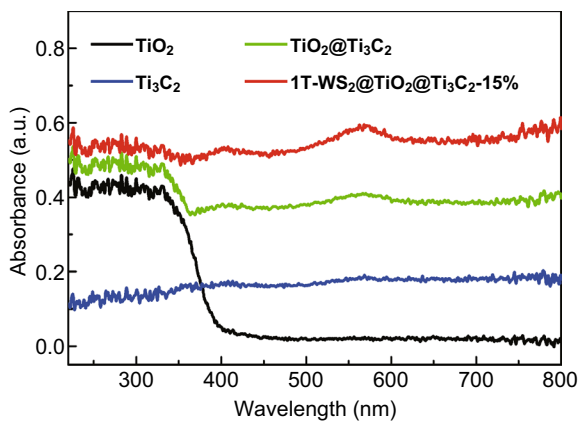


Fig. 5 UV–Vis DRS spectra of Ti₃C₂ MXene, TiO₂ NSs, TiO₂@Ti₃C₂, and 1T-WS₂@TiO₂@Ti₃C₂ composites (15 wt% WS₂)

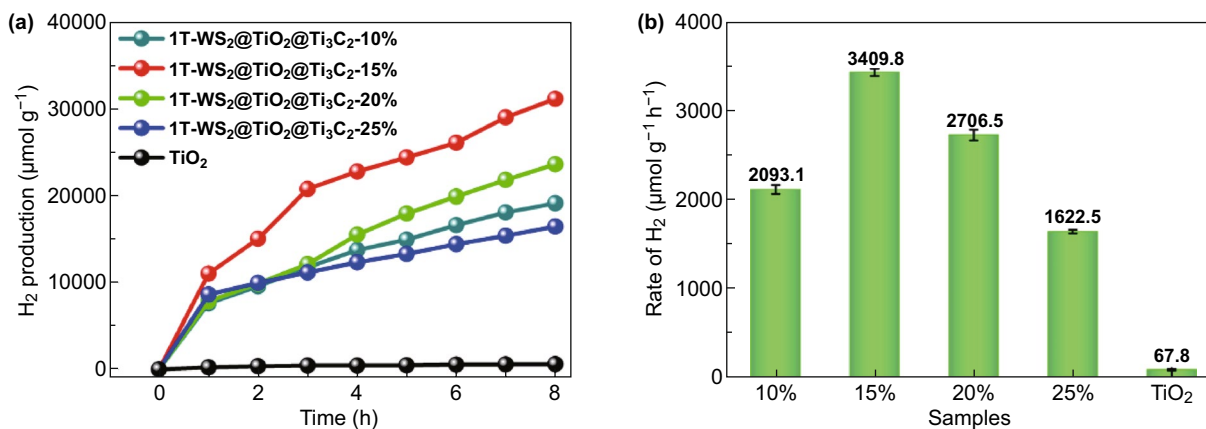


Fig. 6 **a** Photocatalytic H₂ production and **b** rate of the samples under simulated sunlight illumination

Besides, we evaluate the apparent quantum efficiency (AQE) of photocatalysts under the same light source. Table S2 displays the comparison of AQE values of TiO_2 NSs and $1\text{T-WS}_2@ \text{TiO}_2@ \text{Ti}_3\text{C}_2$ composites with different WS_2 ratios (10, 15, 20, and 25 wt%): 0.049% (TiO_2 NSs) < 1.173% ($1\text{T-WS}_2@ \text{TiO}_2@ \text{Ti}_3\text{C}_2$ -25 wt%) < 1.513% ($1\text{T-WS}_2@ \text{TiO}_2@ \text{Ti}_3\text{C}_2$ -10 wt%) < 1.956% ($1\text{T-WS}_2@ \text{TiO}_2@ \text{Ti}_3\text{C}_2$ -20 wt%) < 2.464% ($1\text{T-WS}_2@ \text{TiO}_2@ \text{Ti}_3\text{C}_2$ -15 wt%), which is in accordance with photocatalytic H_2 evolution performance. Moreover, we conduct stability of $1\text{T-WS}_2@ \text{TiO}_2@ \text{Ti}_3\text{C}_2$ composites (15 wt% WS_2) for 24 h (Fig. S7). No noticeable H_2 production decrease is detected after 3 cycles (24 h). SEM images (Fig. S8) and XRD pattern (Fig. S9) of $1\text{T-WS}_2@ \text{TiO}_2@ \text{Ti}_3\text{C}_2$ composites after 3 cycles display no evident difference compared with fresh samples. The results further demonstrate that $1\text{T-WS}_2@ \text{TiO}_2@ \text{Ti}_3\text{C}_2$ composites can act as a favorable photocatalyst for H_2 production. We also delaminated the multilayered Ti_3C_2 MXenes to get monolayered Ti_3C_2 nanosheets (Fig. S10). The XRD pattern of $\text{TiO}_2@ \text{Ti}_3\text{C}_2$ (monolayer) does not detect the diffraction peak of Ti_3C_2 (Fig. S10a). Since Ti_3C_2 monolayer is in full contact with the reaction solution, all Ti_3C_2 may be converted into TiO_2 under the same experimental conditions. As shown in Fig. S10b, $1\text{T-WS}_2@ \text{Ti}_3\text{C}_2@ \text{Ti}_3\text{C}_2$ (monolayer) presents worse photocatalytic H_2 production activity than that of $1\text{T-WS}_2@ \text{TiO}_2@ \text{Ti}_3\text{C}_2$ (multilayer), which demonstrates that the lack of Ti_3C_2 by oxidation in $1\text{T-WS}_2@ \text{Ti}_3\text{C}_2@ \text{Ti}_3\text{C}_2$ (monolayer) greatly affects the photocatalytic H_2 production. Furthermore, changing the ratio between Ti_3C_2 and TiO_2 also affecting the photocatalytic performance of $1\text{T-WS}_2@ \text{TiO}_2@ \text{Ti}_3\text{C}_2$

composites (Fig. S11). Compared with in situ loading of TiO_2 nanosheets (Fig. S12), foreign titanium sources do not improve the photocatalytic performance of $1\text{T-WS}_2@ \text{TiO}_2@ \text{Ti}_3\text{C}_2$ composites, which may be caused by the non-close contact between TiO_2 and Ti_3C_2 caused by the foreign titanium sources.

The introduction of Ti_3C_2 MXene and 1T-WS_2 in $1\text{T-WS}_2@ \text{TiO}_2@ \text{Ti}_3\text{C}_2$ composites would be believed to influence photoinduced carrier separation, which could be characterized by steady and time-resolved PL spectroscopy (Fig. 7). As illustrated in Fig. 7a, TiO_2 NSs possess a high PL peak, resulting in the quick photoinduced carrier recombination. When Ti_3C_2 MXene and 1T-WS_2 are incorporated, the PL peak is significantly reduced (Fig. 7a). Evidently, the photoinduced carrier recombination of TiO_2 is hindered by migrating electrons to Ti_3C_2 and 1T-WS_2 as electron acceptors [44]. An increased lifetime of charge carriers is also detected by loading Ti_3C_2 MXene and 1T-WS_2 (Fig. 7b). The intensity-average lifetimes (τ) of TiO_2 NSs are 0.1138 ns, much shorter than that of $1\text{T-WS}_2@ \text{TiO}_2@ \text{Ti}_3\text{C}_2$ composites (1.2750 ns). The increased carrier lifetime of $1\text{T-WS}_2@ \text{TiO}_2@ \text{Ti}_3\text{C}_2$ composites is beneficial for enhanced carrier separation efficiency.

The photocurrent responses of photocatalysts were prompt by some on-off cycles under light illumination (Fig. 8a). All of samples present reversible photocurrent responses on each irradiation. The photocurrent intensity of $1\text{T-WS}_2@ \text{TiO}_2@ \text{Ti}_3\text{C}_2$ composites is much higher than that of pure TiO_2 NSs, which is due to Ti_3C_2 and 1T-WS_2 as co-catalysts more effectively receiving photoexcited electrons of TiO_2 . The $1\text{T-WS}_2@ \text{TiO}_2@ \text{Ti}_3\text{C}_2$ composites

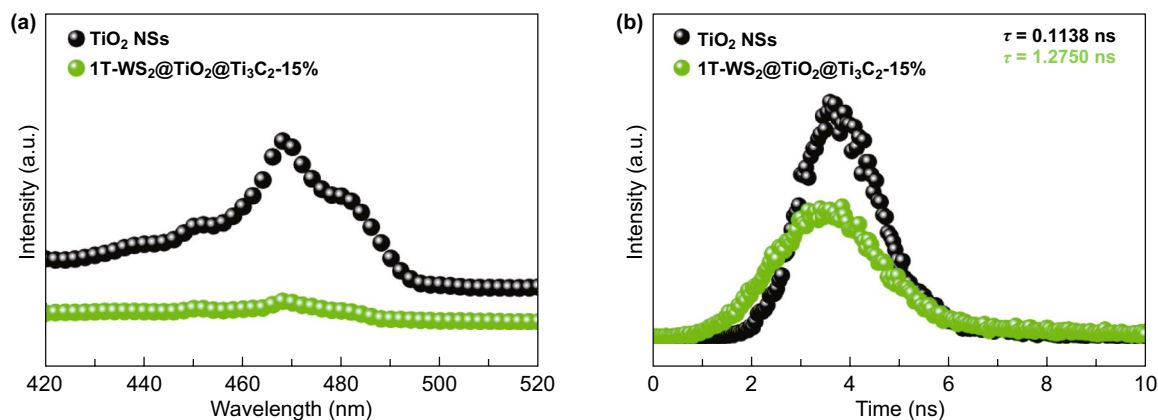


Fig. 7 **a** Steady and **b** time-resolved PL spectra of TiO_2 NSs and $1\text{T-WS}_2@ \text{TiO}_2@ \text{Ti}_3\text{C}_2$ composites (15 wt% WS_2), $\lambda_{\text{ex}} = 325$ nm

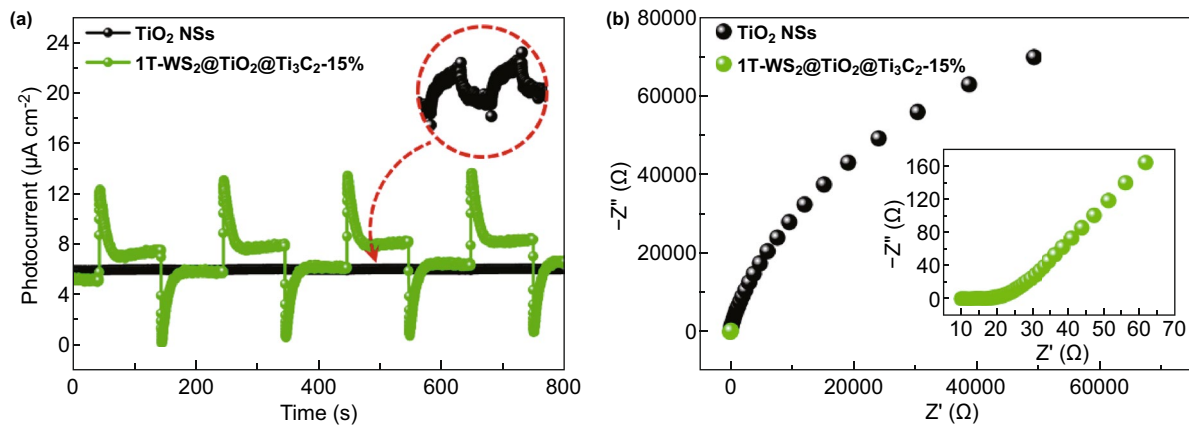


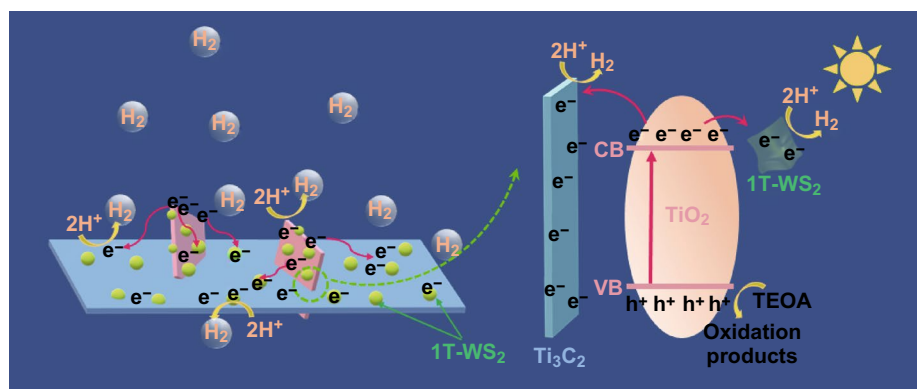
Fig. 8 **a** Transient photocurrent responses and **b** EIS of TiO₂ NSs and 1T-WS₂@TiO₂@Ti₃C₂ composites (15 wt% WS₂)

(Fig. 8b) exhibit a smaller arc radius compared with TiO₂ NSs under light irradiation, suggesting that the 1T-WS₂@TiO₂@Ti₃C₂ composite presents smaller charge transfer resistance, finally causing higher photoexcited carrier transfer and separation efficiency [45].

As shown in Scheme 2, under light irradiation, TiO₂ NSs can be excited to produce electrons and holes. The majority of photoexcited electrons in conduction band (CB) of TiO₂ could instantly migrate to metallic Ti₃C₂ MXene and 1T-WS₂ through the interface. As the photoelectron receivers, Ti₃C₂ MXene and 1T-WS₂ serves as active sites for H₂ production [46, 47]. Meanwhile, the holes in the valence band (VB) of TiO₂ are consumed by the sacrificial reagents. Consequently, the photoexcited carriers are efficiently transferred and separated with the assistance of double co-catalysts Ti₃C₂ and 1T-WS₂.

4 Conclusions

In conclusion, an effective 1T-WS₂@TiO₂@Ti₃C₂ composite photocatalyst is successfully prepared. The development of TiO₂ NSs on Ti₃C₂ MXenes and 1T-WS₂ nanoparticles uniformly distributing on TiO₂@Ti₃C₂ composite is the design concept. The obtained 1T-WS₂@TiO₂@Ti₃C₂ composite with 15 wt% WS₂ loading displays excellent photocatalytic H₂ production performance (3409.8 μmol g⁻¹ h⁻¹), nearly 50 times higher than that of pure TiO₂ NSs. The excellent H₂ evolution performance of 1T-WS₂@TiO₂@Ti₃C₂ composites is ascribed to the following reasons: (1) The introduction of 1T-WS₂ nanoparticles induces enhanced BET surface area and more active sites; (2) Both Ti₃C₂ MXene and 1T-WS₂ possess extraordinary conductivity, which greatly enhance the electron transfer ability and thus achieve highly efficient spatial charge separation.



Scheme 2 Schematic photocatalytic mechanism of 1T-WS₂@TiO₂@Ti₃C₂ composites

Acknowledgements The authors are thankful for fundings from the National Natural Science Foundation of China (Nos. 51872173 and 51772167), Taishan Scholarship of Young Scholars (No. tsqn201812068), Natural Science Foundation of Shandong Province (No. ZR2017JL020), Taishan Scholarship of Climbing Plan (No. tspd20161006), and Key Research and Development Program of Shandong Province (No. 2018GGX102028).

Open Access This article is licensed under a Creative Commons Attribution 4.0 International License, which permits use, sharing, adaptation, distribution and reproduction in any medium or format, as long as you give appropriate credit to the original author(s) and the source, provide a link to the Creative Commons licence, and indicate if changes were made. The images or other third party material in this article are included in the article's Creative Commons licence, unless indicated otherwise in a credit line to the material. If material is not included in the article's Creative Commons licence and your intended use is not permitted by statutory regulation or exceeds the permitted use, you will need to obtain permission directly from the copyright holder. To view a copy of this licence, visit <http://creativecommons.org/licenses/by/4.0/>.

Electronic supplementary material The online version of this article (<https://doi.org/10.1007/s40820-019-0339-0>) contains supplementary material, which is available to authorized users.

References

1. S.W. Boettcher, E.L. Warren, M.C. Putnam, E.A. Santori, D.T. Evans et al., Photoelectrochemical hydrogen evolution using Si microwire arrays. *J. Am. Chem. Soc.* **133**, 1216–1219 (2011). <https://doi.org/10.1021/ja108801m>
2. J. Choi, S.Y. Ryu, W. Balcerski, T.K. Lee, M.R. Hoffmann, Photocatalytic production of hydrogen on Ni/NiO/KNbO₃/CdS nanocomposites using visible light. *J. Mater. Chem.* **18**, 2371–2378 (2008). <https://doi.org/10.1039/B718535A>
3. M.R. Gholipour, C.T. Dinh, F. B eland, T.O. Do, Nanocomposite heterojunctions as sunlight-driven photocatalysts for hydrogen production from water splitting. *Nanoscale* **7**, 8187–8208 (2015). <https://doi.org/10.1039/C4NR07224C>
4. Z. Li, B. Tian, W. Zhen, Y. Wu, G. Lu, Inhibition of hydrogen and oxygen recombination using oxygen transfer reagent hemin chloride in Pt/TiO₂ dispersion for photocatalytic hydrogen generation. *Appl. Catal. B-Environ.* **203**, 408–415 (2017). <https://doi.org/10.1016/j.apcatb.2016.10.049>
5. Z. Liang, X. Bai, P. Hao, Y. Guo, Y. Xue, J. Tian, H. Cui, Full solar spectrum photocatalytic oxygen evolution by carbon-coated TiO₂ hierarchical nanotubes. *Appl. Catal. B* **243**, 711–720 (2019). <https://doi.org/10.1016/j.apcatb.2018.11.017>
6. X. Zhang, Y. Wang, B. Liu, Y. Sang, L. Hong, Heterostructures construction on TiO₂ nanobelts: a powerful tool for building high-performance photocatalysts. *Appl. Catal. B* **202**, 620–641 (2017). <https://doi.org/10.1016/j.apcatb.2016.09.068>
7. Y. Cao, Y. Saygili, A. Ummadisingu, J.L. Teuscher, J. Luo, N. Pellet, F. Giordano, S.M. Zakeeruddin, J.E. Moser, M. Freitag, 11% efficiency solid-state dye-sensitized solar cells with copper (II/I) hole transport materials. *Nat. Commun.* **8**, 15390 (2017). <https://doi.org/10.1038/ncomms15390>
8. N. Michael, Alkaline earth metal oxide nanocluster modification of rutile TiO₂ (110) promotes water activation and CO₂ chemisorption. *J. Mater. Chem. A* **6**, 9451–9466 (2018). <https://doi.org/10.1039/C8TA01789A>
9. J. Jiao, Y. Wei, Y. Zhao, Z. Zhao, A. Duan et al., AuPd/3DOM-TiO₂ catalysts for photocatalytic reduction of CO₂: high efficient separation of photogenerated charge carriers. *Appl. Catal. B* **209**, 228–239 (2017). <https://doi.org/10.1016/j.apcatb.2017.02.076>
10. S. Ma, Y. Deng, J. Xie, K. He, W. Liu, X. Chen, X. Li, Noble-metal-free Ni₃C cocatalysts decorated CdS nanosheets for high-efficiency visible-light-driven photocatalytic H₂ evolution. *Appl. Catal. B* **227**, 218–228 (2018). <https://doi.org/10.1016/j.apcatb.2018.01.031>
11. Y.J. Yuan, D. Chen, J. Zhong, L.X. Yang, J. Wang et al., Interface engineering of a noble-metal-free 2D-2D MoS₂/Cu-ZnIn₂S₄ photocatalyst for enhanced photocatalytic H₂ production. *J. Mater. Chem. A* **5**, 15771–15779 (2017). <https://doi.org/10.1039/C7TA04410K>
12. Y.J. Yuan, H.W. Lu, Z.T. Yu, Z.G. Zou, Noble-metal-free molybdenum disulfide cocatalyst for photocatalytic hydrogen production. *ChemSuschem* **8**, 4113–4127 (2016). <https://doi.org/10.1002/cssc.201501203>
13. Y. Sun, X. Meng, Y. Dall'Agnese, C. Dall'Agnese, S. Duan, Y. Gao, G. Chen, X.F. Wang, 2D MXenes as co-catalysts in photocatalysis: synthetic methods. *Nano-Micro Lett.* **11**, 79 (2019). <https://doi.org/10.1007/s40820-019-0309-6>
14. M. Naguib, V.N. Mochalin, M.W. Barsoum, Y. Gogotsi, 25th anniversary article: MXenes: a new family of two-dimensional materials. *Adv. Mater.* **26**, 992–1005 (2014). <https://doi.org/10.1002/adma.201304138>
15. Z. Li, F. Wu, J. Yu, Q. Deng, F. Zhang, W. Guan, Titanium carbide (Ti₃C₂T_x) MXene: a novel precursor to amphiphilic carbide-derived graphene quantum dots for fluorescent ink, light-emitting composite and bioimaging. *Carbon* **118**, 50–57 (2017). <https://doi.org/10.1016/j.carbon.2017.03.023>
16. X. Xie, M.Q. Zhao, B. Anasori, K. Maleski, C.E. Ren, J. Li, B.W. Byles, E. Pomerantseva, G. Wang, Y. Gogotsi, Porous heterostructured MXene/carbon nanotube composite paper with high volumetric capacity for sodium-based energy storage devices. *Nano Energy* **26**, 513–523 (2016). <https://doi.org/10.1016/j.nanoen.2016.06.005>
17. Y. Li, X. Deng, J. Tian, Z. Liang, H. Cui, Ti₃C₂ MXene-derived Ti₃C₂/TiO₂ nanoflowers for noble-metal-free photocatalytic overall water splitting. *Appl. Mater. Today* **13**, 217–227 (2018). <https://doi.org/10.1016/j.apmt.2018.09.004>
18. J. Pang, R.G. Mendes, A. Bachmatiuk, L. Zhao, H.Q. Ta et al., Applications of 2D MXenes in energy conversion and storage systems. *Chem. Soc. Rev.* **48**, 72–133 (2019). <https://doi.org/10.1039/C8CS00324F>

19. J. Yi, X. She, Y. Song, M. Mao, K. Xia et al., Solvothermal synthesis of metallic 1T-WS₂: a supporting co-catalyst on carbon nitride nanosheets toward photocatalytic hydrogen evolution. *Chem. Eng. J.* **335**, 282–289 (2018). <https://doi.org/10.1016/j.cej.2017.10.125>
20. J.M. Woods, Y. Jung, Y. Xie, W. Liu, Y. Liu, H. Wang, J.J. Cha, One-step synthesis of MoS₂/WS₂ layered heterostructures and catalytic activity of defective transition metal dichalcogenide films. *ACS Nano* **10**, 2004–2009 (2016). <https://doi.org/10.1021/acsnano.5b06126>
21. X. Tong, Y. Qi, J. Chen, N. Wang, Q. Xu, Supercritical CO₂-assisted reverse-micelle-induced solution-phase fabrication of two-dimensional metallic 1T-MoS₂ and 1T-WS₂. *ChemNanoMat* **3**, 466–471 (2017). <https://doi.org/10.1002/cnma.201700011>
22. M. Piao, J. Chu, X. Wang, Y. Chi, H. Zhang, C. Li, H. Shi, M.K. Joo, Hydrothermal synthesis of stable metallic 1T phase WS₂ nanosheets for thermoelectric application. *Nanotechnology* **29**, 025705 (2017). <https://doi.org/10.1088/1361-6528/aa9bfe>
23. Q. Liu, X. Li, Z. Xiao, Y. Zhou, H. Chen et al., Stable metallic 1T-WS₂ nanoribbons intercalated with ammonia ions: the correlation between structure and electrical/optical properties. *Adv. Mater.* **27**, 4837–4844 (2015). <https://doi.org/10.1002/adma.201502134>
24. U. Maitra, U. Gupta, M. De, R. Datta, A. Govindaraj, C.N. Rao, Highly effective visible-light-induced H₂ generation by single-layer 1T-MoS₂ and a nanocomposite of few-layer 2H-MoS₂ with heavily nitrogenated graphene. *Angew. Chem. Int. Ed.* **52**, 13057–13061 (2013). <https://doi.org/10.1002/anie.201306918>
25. H. Yu, P. Xiao, P. Wang, J. Yu, Amorphous molybdenum sulfide as highly efficient electron-cocatalyst for enhanced photocatalytic H₂ evolution. *Appl. Catal. B* **193**, 217–225 (2016). <https://doi.org/10.1016/j.apcatb.2016.04.028>
26. X.B. Li, Y.J. Gao, H.L. Wu, Y. Wang, Q. Guo et al., Assembling metallic 1T-MoS₂ nanosheets with inorganic-ligand stabilized quantum dots for exceptional solar hydrogen evolution. *Chem. Commun.* **53**, 5606–5609 (2017). <https://doi.org/10.1039/C7CC02366A>
27. Y. Li, Z. Yin, G. Ji, Z. Liang, Y. Xue, Y. Guo, J. Tian, X. Wang, H. Cui, 2D/2D/2D heterojunction of Ti₃C₂ MXene/MoS₂ nanosheets/TiO₂ nanosheets with exposed (001) facets toward enhanced photocatalytic hydrogen production activity. *Appl. Catal. B* **246**, 12–20 (2019). <https://doi.org/10.1016/j.apcatb.2019.01.051>
28. M.A. Lukowski, A.S. Daniel, F. Meng, A. Forticaux, L. Li, S. Jin, Enhanced hydrogen evolution catalysis from chemically exfoliated metallic MoS₂ nanosheets. *J. Am. Chem. Soc.* **135**, 10274–10277 (2013). <https://doi.org/10.1021/ja404523s>
29. M. Naguib, M. Kurtoglu, V. Presser, J. Lu, J. Niu, H. Min, L. Hultman, Y. Gogotsi, M.W. Barsoum, Two-dimensional nanocrystals: two-dimensional nanocrystals produced by exfoliation of Ti₃AlC₂. *Adv. Mater.* **37**, 4207 (2011). <https://doi.org/10.1002/adma.201190147>
30. C.C.M. Martinez, A. Ambrosi, A.Y.S. Eng, Z. Sofer, M. Pumera, Metallic 1T-WS₂ for selective impedimetric vapor sensing. *Adv. Funct. Mater.* **25**, 5611–5616 (2015). <https://doi.org/10.1002/adfm.201502223>
31. J. Tian, X. Hu, N. Wei, Y. Zhou, X. Xu, H. Cui, H. Liu, RuO₂/TiO₂ nanobelt heterostructures with enhanced photocatalytic activity and gas-phase selective oxidation of benzyl alcohol. *Sol. Energ. Mat. Sol. C* **151**, 7–13 (2016). <https://doi.org/10.1016/j.solmat.2016.02.017>
32. X. Hu, S. Lu, J. Tian, N. Wei, X. Song, X. Wang, H. Cui, The selective deposition of MoS₂ nanosheets onto (101) facets of TiO₂ nanosheets with exposed (001) facets and their enhanced photocatalytic H₂ production. *Appl. Catal. B* **241**, 329–337 (2019). <https://doi.org/10.1016/j.apcatb.2018.09.051>
33. P. Lian, Y. Dong, Z. Wu, S. Zheng, X. Wang, S. Wang, C. Sun, J. Qin, X. Shi, X. Bao, Alkalized Ti₃C₂ MXene nanoribbons with expanded interlayer spacing for high-capacity sodium and potassium ion batteries. *Nano Energy* **40**, 1–8 (2017). <https://doi.org/10.1016/j.nanoen.2017.08.002>
34. T.A.J. Loh, D.H.C. Chua, Origin of hybrid 1T- and 2H-WS₂ ultrathin layers by pulsed laser deposition. *J. Phys. Chem. C* **49**, 27496–27504 (2015). <https://doi.org/10.1021/acs.jpcc.5b09277>
35. B. Mahler, V. Hoepfner, K. Liao, G.A. Ozin, Colloidal synthesis of 1T-WS₂ and 2H-WS₂ nanosheets: applications for photocatalytic hydrogen evolution. *J. Am. Chem. Soc.* **136**, 14121–14127 (2014). <https://doi.org/10.1021/ja506261t>
36. F. Yang, Z. Ning, H. Liu, Fractal characteristics of shales from a shale gas reservoir in the Sichuan Basin. *China Fuel* **115**, 378–384 (2014). <https://doi.org/10.1016/j.fuel.2013.07.040>
37. Y. Cui, G. Zhang, Z. Lin, X. Wang, Condensed and low-defected graphitic carbon nitride with enhanced photocatalytic hydrogen evolution under visible light irradiation. *Appl. Catal. B* **181**, 413–419 (2016). <https://doi.org/10.1016/j.apcatb.2015.08.018>
38. H. Yang, J. Tian, Y. Bo, Y. Zhou, X. Wang, H. Cui, Visible photocatalytic and photoelectrochemical activities of TiO₂ nanobelts modified by In₂O₃ nanoparticles. *J. Colloid Interf. Sci.* **487**, 258–265 (2017). <https://doi.org/10.1016/j.jcis.2016.10.051>
39. J. Ran, G. Gao, F. Li, T. Ma, A. Du, S. Qiao, Ti₃C₂ MXene cocatalyst on metal sulfide photo-absorbers for enhanced visible-light photocatalytic hydrogen production. *Nat. Commun.* **8**, 13907 (2017). <https://doi.org/10.1038/ncomms13907>
40. L. Yao, N. Zhang, Y. Wang, Y. Ni, Facile formation of 2D Co₂P@Co₃O₄ microsheets through in situ topotactic conversion and surface corrosion: bifunctional electrocatalysts towards overall water splitting. *J. Power Sources* **374**, 142–148 (2018). <https://doi.org/10.1016/j.jpowsour.2017.11.028>
41. A.N. Enyashin, A.L. Ivanovskii, Structural and electronic properties and stability of MXenes Ti₂C and Ti₃C₂ functionalized by methoxy groups. *J. Phys. Chem. C* **117**, 13637–13643 (2013). <https://doi.org/10.1021/jp401820b>
42. T.A.J. Loh, M. Tanemura, D.H.C. Chua, Ultrathin MoS₂ and WS₂ layers on silver nano-tips as electron emitters. *Appl. Phys. Lett.* **109**, 133102 (2016). <https://doi.org/10.1063/1.4963260>



43. H.E. Kim, J. Lee, H. Lee, C. Lee, Synergistic effects of TiO₂ photocatalysis in combination with fenton-like reactions on oxidation of organic compounds at circumneutral pH. *Appl. Catal. B* **116**, 219–224 (2012). <https://doi.org/10.1016/j.apcatb.2011.12.027>
44. M. Schwartzman, V. Sidorov, D. Ritter, Y. Paz, Surface passivation of (100) InP by organic thiols and polyimide as characterized by steady-state photoluminescence. *Semicond. Sci. Technol.* **16**, 68–71 (2001). <https://doi.org/10.1088/0268-1242/16/10/103>
45. Y. Liu, W. Wang, Y. Wang, X. Peng, Homogeneously assembling like-charged WS₂ and GO nanosheets lamellar composite films by filtration for highly efficient lithium ion batteries. *Nano Energy* **7**, 25–32 (2014). <https://doi.org/10.1016/j.nanoen.2014.04.018>
46. A. Manikandan, P.R. Ilango, C.W. Chen, Y.C. Wang, Y.C. Shih et al., A superior dye adsorbent towards the hydrogen evolution reaction combining active sites and phase-engineering of (1T/2H) MoS₂/α-MoO₃ hybrid heterostructured nanoflowers. *J. Mater. Chem. A* **6**, 15320 (2018). <https://doi.org/10.1039/C8TA02496K>
47. X. An, W. Wang, J. Wang, H. Duan, J. Shi, X. Yu, The synergistic effects of Ti₃C₂ MXene and Pt as co-catalysts for highly efficient photocatalytic hydrogen evolution over g-C₃N₄. *Phys. Chem. Chem. Phys.* **20**, 11405–11411 (2018). <https://doi.org/10.1039/C8CP01123K>